Droplet mobility on lubricant-impregnated surfaces

Citation: Smith, J. David et al. "Droplet Mobility on Lubricant-impregnated Surfaces." Soft Matter 9.6 (2013): 1772.

As Published: http://dx.doi.org/10.1039/C2SM27032C

Publisher: Royal Society of Chemistry, The

Persistent URL: http://hdl.handle.net/1721.1/79068

Version: Author's final manuscript: final author's manuscript post peer review, without publisher's formatting or copy editing

Droplet mobility on lubricant-impregnated surfaces

J. David Smith,[a†] Rajeev Dhiman,[a†] Sushant Anand,[a] Ernesto Reza-Garduno,[a] Robert E. Cohen,[b] Gareth H. McKinley,[a] and Kripa K. Varanasi*[a]

Received (in XXX, XXX) Xth XXXXXXXXX 20XX, Accepted Xth XXXXXXXXX 20XX
DOI: 10.1039/b000000x

Non-wetting surfaces containing micro/nanotextures impregnated with lubricating liquids have recently been shown to exhibit superior non-wetting performance compared to superhydrophobic surfaces that rely on stable air-liquid interfaces. Here we examine the fundamental physiochemical hydrodynamics that arise when droplets, immiscible with the lubricant, are placed on and allowed to move along these surfaces. We find that these four-phase systems show novel contact line morphology comprising a finite annular ridge of lubricant pulled above the surface texture and consequently as many as three distinct 3-phase contact lines. We show that these distinct morphologies not only govern the contact line pinning that controls droplets' initial resistance to movement but also the level of viscous dissipation and hence their sliding velocity once the droplets begin to move.

[†]*equal contribution*
[a]*Department of Mechanical Engineering, Massachusetts Institute of Technology, Cambridge, Massachusetts, USA. Tel: +1-617-324-5608; E-mail: varanasi@mit.edu*
[b]*Department of Chemical Engineering, Massachusetts Institute of Technology, Cambridge, Massachusetts, USA.*

† Electronic Supplementary Information (ESI) available: Substrate preparation methods, laser confocal fluorescence microscopy procedure, contact angle and interfacial tension measurements and calculated spreading coefficients, SEM images of ionic liquid impregnated nanograss, video of droplet rolling showing the wetting ridge, videos of droplets rolling demonstrating the effect of lubricant viscosity. See DOI: 10.1039/b000000x/

Introduction

Surfaces with designed chemistry and roughness possess remarkable non-wetting properties, which can be extremely useful in a wide variety of commercial and technological applications.[1-5] Inspired by nature,[6, 7] these properties originate from the diminished contact of the surface with the liquid by trapping air pockets within the texture; as long as these air pockets are stable, the surface continues to exhibit non-wetting behaviour.[8] Maintaining stable air pockets, however, is challenging: the air pockets can be collapsed by external wetting pressures[8-11], can diffuse away into the surrounding liquid [12-14], can lose robustness upon damage to the texture[1, 5] and may be displaced by low surface tension liquids unless special texture design is implemented.[3] Furthermore, condensation or frost nuclei, which can form at the nanoscale throughout the texture, can completely transform the wetting properties and render the textured surface highly wetting[15-18].

A different approach to achieve non-wetting properties involves surfaces containing pockets of a lubricating liquid rather than of air [19]. Stabilized by the capillary forces arising from the microscopic texture, the lubricant – provided it wets the solid preferentially – lets the droplet above it move with remarkable ease as evidenced by the extremely-low contact angle hysteresis (~ 1°) of the droplet.[19] In addition to low hysteresis, recent studies have demonstrated that such non-wetting surfaces can provide self-cleaning properties [20], withstand high drop impact pressures [21], self-heal by capillary wicking upon damage [21], repel a variety of liquids [21], and reduce ice adhesion [22].

Although these studies have demonstrated the potential of the lubricant-impregnated surfaces, several fundamental questions remain unanswered. For example, since there are four distinct phases in this system (the lubricant, the surrounding gas, and the liquid that needs to be shed – referred hereafter for simplicity as oil, air, and water, respectively – plus the textured solid), understanding how the interactions among them determine the morphology of the contact line is non-trivial. This is important because contact line morphology governs droplet pinning and hence its mobility on the surface.[23] Another fundamental question arises from the fact that previous studies have relied on the texture being completely submerged in oil in order to achieve low hysteresis. Although complete submergence may be achieved temporarily by depositing excess oil [21], eventually this excess will drain away (e.g. under gravity) and the oil-air interface may contact the textured solid. At that point, complete submergence is possible only if the oil is able to completely wet the texture, i.e. $\theta_{os(a)} = 0^\circ$ which is the contact angle of oil (subscript '*o*') on the textured solid (subscript '*s*') in the presence of air (subscript '*a*'). The situation is further complicated once a water droplet is placed on the oil-impregnated surface, which now will remain submerged in oil only if $\theta_{os(w)} = 0^\circ$ as well, where the subscript '*w*' refers to water. It is important to determine whether satisfying both $\theta_{os(a)} = 0^\circ$ and $\theta_{os(w)} = 0^\circ$ are essential because such a requirement may severely restrict the choice of oils that can be used for a given droplet liquid and textured substrate material. Another important question is determining the key factors, including the role of the oil viscosity, that affect how droplets are shed – whether they roll or slip – and what their shedding velocities are. Moreover, questions related to the longevity of the impregnated oil film and its possible depletion, due to evaporation and entrainment with the droplets being shed, have not been thoroughly addressed.

In this paper we investigate these fundamental aspects of lubricant-impregnated surfaces, identify the principles governing droplet mobility on them, and provide guidelines for their design. To unambiguously determine the performance of these surfaces, we prepared them in a repeatable manner by carefully dipping the dry textured substrates into a bath of oil and removing it at a controlled rate so that there was no excess oil (see Supplementary Material).[24] The textured substrates consisted of a

lithographically-patterned silicon micropost array. The texture was coated with a low surface energy silane (octadecyltrichlorosilane – OTS which exhibits an advancing water contact angle of 110 ± 4 ° on a smooth substrate) in order to render it hydrophobic and hence preferentially wetted by oil. Although not recognized in previous studies[20, 21], the oil may spread over and "cloak" the water droplet (Fig 1a). This is important because cloaking can cause the progressive loss of impregnated oil through entrainment in the water droplets as they are shed from the surface. The criterion for cloaking is given by the spreading coefficient, $S_{ow(a)} \equiv \gamma_{wa} - \gamma_{wo} - \gamma_{oa}$, where γ is the interfacial tension between the two phases designated by subscripts w, o, and a.[25] Thus, $S_{ow(a)} > 0$ implies that the oil will cloak the water droplet (Fig. 1a), whereas $S_{ow(a)} < 0$ implies otherwise (Fig. 1b). Based on this criterion, we chose two different liquids: silicone oil, for which $S_{ow(a)} \approx 6$ mN/m (see supplementary materials) and an ionic liquid (1-butyl-3-methylimidazolium bis(trifluoromethylsulfonyl) imide - BMIm) for which $S_{ow(a)} \approx -5$ mN/m [26]. Ionic liquids have extremely low vapour pressures (~10^{-12} mmHg)[27], and therefore they mitigate the concern of the lubricant loss through evaporation. Goniometric measurements of the advancing and receding contact angles of these liquids in the presence of air and water as well as their interfacial tensions were performed and are presented in Tables S1 and S2 (see Supplementary Material).

Figure 1c shows an 8 µl water droplet placed on the silicone oil impregnated texture. The droplet forms a large apparent contact angle (~100˚) but very close to the solid surface (red arrows in Fig. 1c), its profile changes from convex to concave. When a fluorescent dye was added to the silicone oil and imaged under UV light, the point of inflection corresponded to the height to which an annular ridge of oil was pulled up in order to satisfy a vertical force balance of the interfacial tensions at the inflection point (Fig. 1e). Although the oil should spread over the entire droplet (Fig. 1c), the cloaking film was too thin to be captured in these images. The "wetting ridge" was also observed in the case of ionic liquid (Fig. 1d, f). Later, we will demonstrate the importance of the wetting ridge to droplet mobility. Such wetting ridges are reminiscent of those observed around droplets on soft substrates.[28-31]

As mentioned earlier, the texture can be completely submerged in the oil if $\theta_{os(a)} = 0^\circ$. This condition was found to be true for silicone oil, implying that the tops of the posts should be covered by a stable thin oil film. This film was observed experimentally using laser confocal fluorescence microscopy (LCFM); the post tops appear bright due to the presence of a fluorescent dye that was dissolved in the oil (Fig. 1g). Environmental SEM images of the surface (Fig. 1i) show the oil-filled texture and confirm that this film is less than a few microns thick, consistent with prior estimates of completely-wetting films.[32] On the other hand, BMIm has a non-zero contact angle on a smooth OTS-coated silicon surface ($\theta_{os(a)} = 65 \pm 5^\circ$) indicating that with this lubricant the post tops should remain dry. Indeed, LCFM images confirmed this (Fig. 1h) – the post tops appear dark as there is no dye present to fluoresce. Since BMIm is conductive and has an extremely low vapour pressure, it could be imaged in a SEM. As shown in Fig. 1j, discrete droplets resting on post tops are seen, confirming that a thin film was not stable on the post tops in this case.

The above findings motivate us to systematically determine all possible thermodynamic configurations in which a static droplet can exist on these surfaces. We demonstrate that the stable wetting configuration affects the mobility of droplets. In addition, we investigate the role of texture geometry, the wetting ridge, and the oil viscosity on droplet mobility and develop models to explain the observed behaviour and provide a framework for designing lubricant-impregnated surfaces.

Stable configurations of droplets on lubricant-impregnated surfaces

As shown in Fig. 1b, in the case of BMIm there are three distinct 3-phase contact lines at the perimeter of the drop that confine the wetting ridge: the oil-water-air contact line, the oil-solid-air contact line outside the drop, and the oil-solid-water contact line underneath the drop. These contact lines exist because $\theta_{os(a)} > 0$, $\theta_{os(w)} > 0$, and $S_{ow(a)} < 0$. In contrast, in the case of silicone oil (Fig. 1a), none of these contact lines exist because $\theta_{os(a)} = 0$, $\theta_{os(w)} = 0$, and $S_{ow(a)} > 0$. These configurations are just two of the 12 different configurations in such a four-phase system where oil impregnation is possible. These configurations are discussed below.

We first outline a thermodynamic framework that allows one to predict which of these 12 states will be stable for a given droplet, oil, and substrate material. There are three possible configurations to consider for the interface outside of the droplet (in an air environment), and three possible configurations to consider for the interface underneath the droplet (in a water environment). These configurations are shown in Table 1 along with the total interface energy of each configuration. The configurations possible outside the droplet are *A1* (not impregnated, i.e. dry), *A2* (impregnated with emergent features), and *A3* (impregnated with submerged features – i.e. encapsulated). On the other hand, underneath the droplet, the possible configurations are *W1* (impaled), *W2* (impregnated with emergent features), and *W3* (impregnated with submerged features – i.e. encapsulated). The stable configuration will be the one that has the lowest total interface energy.

We first restrict our attention to the configurations outside of the droplet. Consider a textured surface as it is slowly withdrawn from a reservoir of oil. The resulting surface could be in any of states *A1*, *A2*, and *A3* depending on which has the lowest energy. For example, state *A2* would be stable if it has the lowest total interface energy, i.e. $E_{A2} < E_{A1}, E_{A3}$. From Table 1, this results in:

$$E_{A2} < E_{A1} \quad \Leftrightarrow \quad (\gamma_{sa} - \gamma_{os})/\gamma_{oa} > (1-\phi)/(r-\phi) \qquad (1)$$

$$E_{A2} < E_{A3} \quad \Leftrightarrow \quad \gamma_{sa} - \gamma_{os} - \gamma_{oa} < 0 \qquad (2)$$

where ϕ is the fraction of the projected area of the surface that is occupied by the solid and r is the ratio of total surface area to the projected area of the solid. In the case of square posts with width a, edge-to-edge spacing b, and height h, $\phi = a^2/(a+b)^2$ and $r = 1+4ah/(a+b)^2$. Applying Young's equation, $\cos(\theta_{os(a)}) = (\gamma_{sa}-\gamma_{os})/\gamma_{oa}$, Eq. (1) reduces to the hemi-wicking criterion for the

propagation of a oil through a textured surface[1, 20]: $\cos(\theta_{os(a)}) > (1-\phi)/(r-\phi) = \cos(\theta_c)$. This requirement can be conveniently expressed as $\theta_{os(a)} < \theta_c$. In Eq. (2), $\gamma_{sa} - \gamma_{os} - \gamma_{oa}$, is simply the spreading coefficient $S_{os(a)}$ of oil on the textured surface in the presence of air. We can reorganize this as $(\gamma_{sa} - \gamma_{os}) / \gamma_{oa} < 1$, and applying Young's equation again, Eq. (2) can be written as $\theta_{os(a)} > 0$. Expressing Eq. (1) in terms of the spreading coefficient $S_{os(a)}$, yields: $-\gamma_{oa}(r-1)/(r-\phi) < S_{os(a)}$. The above simplifications then lead to the following equivalent criteria for the surface to be in state *A2*:

$$E_{A2} < E_{A1}, E_{A3} \Leftrightarrow \theta_c > \theta_{os(a)} > 0 \Leftrightarrow -\gamma_{oa}(r-1)/(r-\phi) < S_{os(a)} < 0 \quad (3)$$

Similarly, state *A3* would be stable if $E_{A3} < E_{A2}, E_{A1}$. From Table 1, this gives:

$$E_{A3} < E_{A2} \Leftrightarrow \theta_{os(a)} = 0 \Leftrightarrow \gamma_{sa} - \gamma_{os} - \gamma_{oa} \equiv S_{os(a)} \geq 0 \quad (4)$$

$$E_{A3} < E_{A1} \Leftrightarrow \theta_{os(a)} < \cos^{-1}(1/r) \Leftrightarrow S_{os(a)} > -\gamma_{oa}(1-1/r) \quad (5)$$

Note that Eq. (5) is automatically satisfied by Eq. (4), thus the criterion for state *A3* to be stable (i.e. encapsulation) is given by Eq. (4). Following a similar procedure, the condition for state *A1* to be stable can be derived as:

$$E_{A1} < E_{A2}, E_{A3} \Leftrightarrow \theta_{os(a)} > \theta_c \Leftrightarrow S_{os(a)} < -\gamma_{oa}(r-1)/(r-\phi) \quad (6)$$

Note that the rightmost expression of Eq. (4) can be rewritten as $(\gamma_{sa} - \gamma_{os})/\gamma_{oa} \geq 1$. This raises an important point: Young's equation would suggest that if $\theta_{os(a)} = 0$, then $(\gamma_{sa} - \gamma_{os})\gamma_{oa} = 1$ (i.e. $S_{os(a)} = 0$). However, $\theta_{os(a)} = 0$ is true also for the case that $(\gamma_{sa} - \gamma_{os}) / \gamma_{oa} > 1$ (i.e. $S_{os(a)} > 0$). It is important to realize that Young's equation predicts the contact angle based on balancing the surface tension forces on a contact line – the equality only exists for a contact line *at static equilibrium*. For a spreading film ($S_{os(a)} > 0$) a static contact line doesn't exist, hence precluding the applicability of Young's equation.

We now consider the configurations possible underneath the droplet. Upon contact with water, the interface beneath the droplet will attain one of the three different states – *W1*, *W2*, or *W3* (Table 1) – depending on which has the lowest energy. Applying the same method to determine the stable configurations of the interface beneath the droplet, and using the total interface energies provided in Table 1, the stability requirements take a form similar to Eqs (3), (4), and (6), with γ_{oa}, γ_{sa}, $\theta_{os(a)}$, $S_{os(a)}$, replaced with γ_{ow}, γ_{sw}, $\theta_{os(w)}$, $S_{os(w)}$ respectively. Notice also that θ_c is not affected by the surrounding environment as it is only a function of the texture parameters, ϕ and r. Thus, the texture will remain impregnated with oil beneath the droplet with emergent post tops (i.e. state *W2*) when:

$$E_{W2} < E_{W1}, E_{W3} \Leftrightarrow \theta_c > \theta_{os(w)} > 0 \Leftrightarrow -\gamma_{ow}(r-1)/(r-\phi) < S_{os(w)} < 0 \quad (7)$$

State *W3* will be stable (i.e. the oil will encapsulate the texture) when:

$$E_{W3} < E_{W1}, E_{W2} \Leftrightarrow \theta_{os(w)} = 0 \Leftrightarrow \gamma_{sw} - \gamma_{os} - \gamma_{ow} \equiv S_{os(w)} \geq 0. \quad (8)$$

and the droplet will displace the oil and be impaled by the textures (state *W1*) when:

$$E_{W1} < E_{W2}, E_{W3} \Leftrightarrow \theta_{os(w)} > \theta_c \Leftrightarrow S_{os(w)} < -\gamma_{ow}(r-1)/(r-\phi) \quad (9)$$

Combining the above criteria along with the criterion for cloaking of the water droplet by the oil film described earlier, the various possible states can be organized in a regime map, which is shown Fig. 2. The cloaking criterion is represented by the upper two schematic drawings. For each of these cases, there are six different configurations possible depending on how the oil interacts with the surface texture in the presence of air (vertical axis in Fig. 2) and water (horizontal axis in Fig. 2). The vertical and horizontal axes are the normalized spreading coefficients $S_{os(a)} / \gamma_{oa}$ and $S_{os(w)} / \gamma_{ow}$ respectively. Considering first the vertical axis of Fig. 2, when $S_{os(a)} / \gamma_{oa} < -(r-1)/(r-\phi)$, i.e. when Eq. (6) holds, oil does not even impregnate the texture. As $S_{os(a)} / \gamma_{oa}$ increases above this critical value, impregnation becomes feasible but the post tops are still left emerged. Once $S_{os(a)} / \gamma_{oa} > 0$, the post tops are also submerged in the oil leading to complete encapsulation of the texture. Similarly, on the x-axis of Fig. 2 moving from left to right, as $S_{os(w)} / \gamma_{ow}$ increases, the droplet transitions from an impaled state to an impregnated state to a fully-encapsulated state. Although prior studies[20, 21] have proposed simple criteria for whether a deposited drop would float or sink, additional states, as shown in Fig. 2, were not recognized.

Figure 2 shows that there can be up to three different contact lines, two of which can get pinned on the texture. The degree of pinning determines the roll-off angle α^*, the angle of inclination at which a droplet placed on the textured solid begins to move. Droplets that completely displace the oil (states *A3-W1, A2-W1* in Fig. 2) are not expected to roll off the surface. These states are achieved when $\theta_{os(w)} > \theta_c$ as is the case for both BMI-Im and silicone oil impregnated surfaces when the silicon substrates are not treated with OTS (see supplementary information). As expected, droplets did not roll off of these surfaces. Droplets in states with emergent post tops (*A3-W2*, *A2-W2*, *A2-W3*) are expected to have reduced mobility that is strongly texture dependent, whereas those in states with encapsulated posts outside *and* beneath the droplet (the *A3-W3* states in Fig. 2) are expected to exhibit no pinning and consequently infinitesimally small roll-off angles. To test this hypothesis, we measured roll-off angles of 5 μl droplets on silicone oil and BMIm impregnated textures while varying the post spacing *b*. For comparison, the same textures without a lubricant (i.e. the conventional superhydrophobic case) were also evaluated. The results are shown in Fig. 3a. The silicone oil encapsulated surfaces have extremely low roll-off angles regardless of the post spacing and oil viscosity, showing that contact line pinning was negligible, as predicted for a liquid droplet in an *A3-W3* state with no contact lines on the textured substrate. On the other hand, BMIm impregnated textures showed much higher roll-off angles, which increased as the spacing decreased – a trend that is similar to Cassie droplets on superhydrophobic surfaces.[33] This observation shows that pinning was significant in this case, and occurs on the emergent post tops. (Fig. 3b). However, we were able to significantly reduce this pinning by adding a second smaller length scale texture (i.e. nanograss on the posts), so that BMIm impregnated the texture even on the post tops, thereby substantially reducing ϕ (see Fig. 3c and additional images in Supplementary Material). The roll-off angle decreased from over

30° to only about 2°. It is important to note that the reduction in the emergent area fraction ϕ is not due to the absolute size of the texture features; since the oil-water and oil-air interfaces must intersect surface features at contact angles $\theta_{os(w)}$ and $\theta_{ow(a)}$, ϕ rather depends on these contact angles and feature geometry.

The effect of texture on the roll-off angle can be modelled by balancing gravitational forces with pinning forces. A force balance of a water droplet on a smooth solid surface at incipient motion gives $\rho_w \Omega g \sin\alpha^* \approx 2R_b\gamma_{wa}\,(\cos\theta_{rec,ws(a)} - \cos\theta_{adv,ws(a)})$[34], where ρ_w is the density of the liquid droplet of volume Ω, g is the gravitational acceleration, R_b is the droplet base radius, and $\theta_{adv,ws(a)}$ and $\theta_{rec,ws(a)}$ are the advancing and receding contact angles of droplet in air on the smooth solid surface. To extend this model to our system, we recognize that pinning results from contact angle hysteresis of up to two contact lines : an oil-air-solid contact line with a pinning force per unit length given by γ_{oa} $(\cos\theta_{rec,os(a)} - \cos\theta_{adv,os(a)})$ and an oil-water-solid contact line with a pinning force per unit length given by γ_{ow} $(\cos\theta_{rec,os(w)} - \cos\theta_{adv,os(w)})$. The length of the contact line over which pinning occurs is expected to scale as $R_b\,\phi^{1/2}$ where $\phi^{1/2}$ is the fraction of the droplet perimeter ($\sim R_b$) making contact with the emergent features of the textured substrate. Thus a force balance tangential to the surface gives:

$$\rho_w \Omega g \sin\alpha^* \sim R_b\phi^{1/2}[\gamma_{ow}(\cos\theta_{rec,os(w)} - \cos\theta_{adv,os(w)}) + \gamma_{oa}(\cos\theta_{rec,os(a)} - \cos\theta_{adv,os(a)})] \quad (10)$$

Dividing Eq. (10) by $R_b\gamma_{wa}$ we obtain a non-dimensional expression:

$$Bo\sin\alpha^* f(\theta) \sim \phi^{1/2}[\gamma_{ow}(\cos\theta_{rec,os(w)} - \cos\theta_{adv,os(w)}) + \gamma_{oa}(\cos\theta_{rec,os(a)} - \cos\theta_{adv,os(a)})]/\gamma_{wa} \quad (11)$$

where $f(\theta)=\Omega^{1/3}/R_b=[(\pi/3)(2+\cos\theta)(1-\cos\theta)^2/\sin^3\theta)]^{1/3}$ by assuming the droplet to be a spherical cap making an apparent contact angle θ with the surface.[35] $Bo=\Omega^{2/3}\rho_w g/\gamma_{wa}$ is the Bond number, which compares the relative magnitude of gravitational forces to surface tension forces. Values for $\theta_{rec,os(w)}$, $\theta_{adv,os(w)}$, $\theta_{rec,os(a)}$, $\theta_{adv,os(a)}$, γ_{ow}, γ_{oa}, and γ_{wa} are provided in Tables S1 and S2 of the Supplementary Material. Fig. 3d shows that the measured data is in reasonable agreement with the scaling of Eq. (11). The data for the silicone oil encapsulated surface and for the BMIm impregnated, nanograss-covered posts lie close to the origin as both ϕ and α^* are very small in these cases.

Dynamics of droplet shedding

Once gravitational forces on a droplet overcome the pinning forces, the velocity attained by the droplet determines how quickly it can be shed, which reflects the non-wetting performance of the surface. For a droplet of volume Ω this velocity would be expected to depend on both the contact line pinning and viscosity of the lubricant. We measured the steady-state shedding velocity V of water droplets using a high-speed camera while systematically varying lubricant dynamic viscosity μ_o, post spacing b, substrate tilt angle α, and droplet volume, Ω. These measurements are shown in Fig. 4a where V is plotted as a function of α for different μ_o, b, and Ω; the velocity V, increases with α and Ω as both increase the gravitational force acting on the droplet. However, V decreases with μ_o and ϕ as both increase the resistance to droplet motion (see supplementary video S1).

To explain these trends, we first determine whether the droplet is rolling or sliding. Consider the oil-water interface beneath the droplet as shown in Fig. 4b. The shear stress at this interface, on the water side, scales as $\tau_w \sim \mu_o(V-V_i)/h_{cm}$ and on the oil side scales as $\tau_o \sim \mu_o V_i/t$, where V_i is the velocity of the oil-water interface and h_{cm} is the height of the centre of mass of the droplet above the solid surface, and t is the thickness of the oil film. Since τ_w must be equal to τ_o at the oil-water interface, $\mu_w(V-V_i)/h_{cm} \sim \mu_o V_i/t$. Rearranging this gives:

$$V_i/V \sim \left(1+\frac{\mu_o}{\mu_w}\frac{h_{cm}}{t}\right)^{-1} \quad (12)$$

Since $(\mu_o/\mu_w)(h_{cm}/t) >> 1$ in our experiments, $V_i/V << 1$, i.e. the oil-water interface moves at a negligibly small velocity relative to that of the droplet's centre of mass. This suggests that the droplets being shed in our experiments are rolling. We confirmed this prediction by adding ground coffee particles to the water droplet and tracking their motion relative to the droplet with a high-speed camera as the droplet moved across the surface. Particle trajectories, shown in Fig. 4c, clearly show that the droplets roll across the liquid-impregnated surface as they are shed (μ_o=96.4 cP; also see the supplementary video S2).

To determine the magnitude of V, we balance the rate of change of gravitational potential energy as the droplet rolls down the incline with the total rate of energy dissipation due to contact line pinning and viscous effects. The resulting energy balance gives:

$$V(F_g - F_p) \sim \mu_w \int_{\Omega_{drop}} (\nabla\overline{u})^2_{drop}\, d\Omega + \mu_o \int_{\Omega_{film}} (\nabla\overline{u})^2_{film}\, d\Omega + \mu_o \int_{\Omega_{ridge}} (\nabla\overline{u})^2_{ridge}\, d\Omega \quad (13)$$

where F_g and F_p represent the net gravitational and pinning forces acting on the droplet, the Ω terms are the volume over which viscous dissipation occurs, and the $\nabla\overline{u}$ terms are the corresponding velocity gradients. The form of Eq. (13) is similar to that for viscous droplets rolling on completely non-wetting surfaces[36] though additional terms are present due to the presence of the impregnated oil. The three terms on the right side of Eq. (13) represent the rate of viscous dissipation within the droplet (*I*), in the oil film beneath the droplet (*II*), and in the wetting ridge near the three-phase contact line (*III*).

The rate of viscous dissipation within the droplet (*I*) is primarily confined to the volume beneath its centre of mass[37] and can be approximated as $I \sim \mu_w(V/h_{cm})^2 R_b^2 h_{cm}$, where R_b is the base radius of the droplet. Applying geometrical relations for a spherical cap, $R_b/h_{cm} = g(\theta) = 4/3(\sin\theta)(2+\cos\theta)/(1+\cos\theta)^2$, we get:

$$I \sim \mu_w V^2 R_b g(\theta)$$

The rate of viscous dissipation within the film (*II*) can be approximated as $II \sim \mu_o(V_i/t)^2 R_b^2 t$. Since $(\mu_w/\mu_o)(t/h_{cm}) \ll 1$, from Eq. (12) we can write $\nabla\overline{u}_{film} \sim V_i/t \sim (\mu_w/\mu_o)(V/h_{cm})$. Using $h_{cm} = R_b/g(\theta)$, we get:

$$II \sim \frac{\mu_w^2}{\mu_o} V^2 \left[g(\theta)\right]^2 t$$

Finally, the rate of viscous dissipation in the wetting ridge (*III*) can be approximated as $III \sim \mu_o (V/h_{ridge})^2 R_b h_{ridge}^2$ since fluid velocities within the wetting ridge must scale as the velocity of the centre of mass and vanish at the solid surface, giving velocity gradients that scale as $\nabla \bar{u}_{ridge} \sim V/h_{ridge}$, where h_{ridge} is the height of the wetting ridge. Thus,

$$III \sim \mu_o V^2 R_b .$$

Noting that $F_g = \rho_w \Omega g \sin\alpha$ and $F_p = \rho_w \Omega g \sin\alpha^*$ and dividing both sides of Eq. (13) by $R_b V \gamma_{wa}$ yields

$$Bo\left(\sin\alpha - \sin\alpha^*\right) f(\theta) \sim Ca \left\{ g(\theta) + \left[g(\theta)\right]^2 \frac{\mu_w}{\mu_o} \frac{t}{R_b} + \frac{\mu_o}{\mu_w} \right\} \quad (14)$$

Where $Ca = \mu_w V/\gamma_{wa}$, is the capillary number, $Bo = \Omega^{2/3} \rho_w g/\gamma_{wa}$ is the Bond number, and $f(\theta) = \Omega^{1/3}/R_b$ (defined in the previous section). Since $(\mu_w/\mu_o)(t/R_b) \ll 1$, and $\mu_o/\mu_w \gg g(\theta)$ in our experiments, Eq. (14) can be simplified to:

$$Bo\left(\sin\alpha - \sin\alpha^*\right) f(\theta) \sim Ca \frac{\mu_o}{\mu_w} \quad (15)$$

The datasets shown in Fig. 4a were organized according to Eq. (15) and were found to collapse onto a single curve (Fig. 4d), demonstrating that the above scaling model captures the essential physics of the phenomenon: the gravitational potential energy of the rolling droplet is primarily consumed in viscous dissipation in the wetting ridge around the base of the rolling droplet. Similar conclusions apply to solid spheres rolling on thin films of viscous oil.[38] Furthermore, Eq. (14) and Eq. (15) apply for cloaked and uncloaked droplets, because inertial and gravitational forces in the cloaking films are very small. Consequently, the velocity is uniform across the film and viscous dissipation is negligible.

Conclusions

In summary, we have shown that droplets placed on lubricant-impregnated surfaces exhibit fundamentally different behaviour compared to typical superhydrophobic surfaces. For example, the droplets pull up the impregnated lubricant and can even become completely cloaked by it, which can not only accelerate lubricant depletion from the textured surface but also contaminate the repelled droplets, an outcome that could be undesirable in some applications. Additionally, these unique four-phase systems can have up to three different 3-phase contact lines, giving up to 12 different thermodynamic configurations. In contrast to previous studies on these systems, we find, through direct high-resolution imaging, that the lubricant film encapsulating the texture is stable only if it wets the texture completely ($\theta_{os(a)} = 0$), otherwise portions of the textures dewet and emerge from the lubricant film. Although complete encapsulation of the texture is most desirable in order to eliminate pinning, meeting such a requirement could severely restrict the choice of lubricants. Fortunately, texture geometry and hierarchical features can be exploited to reduce the emergent areas and achieve roll-off angles close to those obtained with fully wetting lubricants. Droplets of low-viscosity liquids, such as water placed on these impregnated surfaces, roll rather than slip with velocities that vary inversely with lubricant viscosity. Our model captures this dependence as well as the effect of other parameters such as droplet and texture size and substrate tilt angle. The model also predicts that the majority of viscous dissipation originates from the wetting ridge, rather than the lubricant film underneath the droplet. Given the above findings, we conclude that lubricant-impregnated surfaces need to be carefully designed in order to deliver optimal non-wetting properties.

References

1. D. Quéré, *Annu Rev Mater Res*, 2008, **38**, 71-99.
2. N. A. Patankar, *Soft Matter*, 2010, **6**, 1613-1620.
3. A. Tuteja, W. Choi, M. L. Ma, J. M. Mabry, S. A. Mazzella, G. C. Rutledge, G. H. McKinley and R. E. Cohen, *Science*, 2007, **318**, 1618-1622.
4. N. J. Shirtcliffe, G. McHale and M. I. Newton, *J Polym Sci Pol Phys*, 2011, **49**, 1203-1217.
5. L. Bocquet and E. Lauga, *Nature Materials*, 2011, **10**, 334-337.
6. W. Barthlott and C. Neinhuis, *Planta*, 1997, **202**, 1-8.
7. X. F. Gao and L. Jiang, *Nature*, 2004, **432**, 36-36.
8. A. Lafuma and D. Quéré, *Nature Materials*, 2003, **2**, 457-460.
9. D. Bartolo, F. Bouamrirene, E. Verneuil, A. Buguin, P. Silberzan and S. Moulinet, *Europhys Lett*, 2006, **74**, 299-305.
10. M. Reyssat, J. M. Yeomans and D. Quéré, *Europhys Lett*, 2008, **81**, 26006.
11. T. Deng, K. K. Varanasi, M. Hsu, N. Bhate, C. Keimel, J. Stein and M. Blohm, *Applied Physics Letters*, 2009, **94**, 133109.
12. R. N. Govardhan, G. S. Srinivas, A. Asthana and M. S. Bobji, *Physics of Fluids*, 2009, **21**, 052001.
13. C. Lee and C. J. Kim, *Physical Review Letters*, 2011, **106**, 014502.
14. N. A. Patankar, *Langmuir*, 2010, **26**, 8783-8786.
15. K. K. Varanasi, M. Hsu, N. Bhate, W. Yang and T. Deng, *Applied Physics Letters*, 2009, **95**, 094101.
16. K. K. Varanasi, T. Deng, J. D. Smith, M. Hsu and N. Bhate, *Applied Physics Letters*, 2010, **97**, 234102-234102.
17. A. J. Meuler, G. H. McKinley and R. E. Cohen, *ACS Nano*, 2010, **4**, 7048-7052.
18. C. Dorrer and J. Ruhe, *Soft Matter*, 2009, **5**, 51-61.
19. D. Quéré, *Reports on Progress in Physics*, 2005, **68**, 2495-2532.
20. A. Lafuma and D. Quéré, *Europhys Lett*, 2011, **96**, 56001.
21. T. S. Wong, S. H. Kang, S. K. Y. Tang, E. J. Smythe, B. D. Hatton, A. Grinthal and J. Aizenberg, *Nature*, 2011, **477**, 443-447.
22. P. Kim, T.-S. Wong, J. Alvarenga, M. J. Kreder, W. E. Adorno-Martinez and J. Aizenberg, *ACS Nano*, 2012, **6**,

6569-6577.
23. J. F. Joanny and P. G. De Gennes, *Journal of Chemical Physics*, 1998, **81**, 552-562.
24. J. Seiwert, C. Clanet and D. Quéré, *Journal of Fluid Mechanics*, 2011, **669**, 55-63.
25. P. G. de Gennes, F. Brochard-Wyart and D. Quéré, *Capillarity and wetting phenomena : drops, bubbles, pearls, waves*, Springer, New York, 2004.
26. S. Anand, A. T. Paxson, J. Smith, R. Dhiman and K. K. Varanasi, APS March Meeting 2012 Boston, MA, 2012.
27. M. Bier and S. Dietrich, *Mol Phys*, 2010, **108**, 211-214.
28. A. Carre, J. C. Gastel and M. E. R. Shanahan, *Nature*, 1996, **379**, 432-434.
29. M. E. R. Shanahan and A. Carre, *Langmuir*, 1995, **11**, 1396-1402.
30. C. W. Extrand and Y. Kumagai, *Journal of Colloid and Interface Science*, 1996, **184**, 191-200.
31. M. Sokuler, G. K. Auernhammer, M. Roth, C. Liu, E. Bonacurrso and H.-J. Butt, *Langmuir*, 2009, **26**, 1544-1547.
32. P. G. de Gennes, *Reviews of Modern Physics*, 1985, **57**, 827-863.
33. K. K. Varanasi, T. Deng, M. F. Hsu and N. Bhate, ASME 2008 International Mechanical Engineering Congress and Exposition Boston, 2008.
34. C. Furmidge, *Journal of Colloid Science*, 1962, **17**, 309-324.
35. D. Quéré, M.-J. Azzopardi and L. Delattre, *Langmuir*, 1998, **14**, 2213-2216.
36. L. Mahadevan and Y. Pomeau, *Physics of Fluids*, 1999, **11**, 2449-2453.
37. N. Moradi, F. Varnik and I. Steinbach, *Europhys Lett*, 2011, **95**, 44003.
38. J. Bico, J. Ashmore-Chakrabarty, G. H. McKinley and H. A. Stone, *Physics of Fluids*, 2009, **21**, 082103.

Table 1. Schematics of wetting configurations outside and underneath the drop (column 2). The total interface energies per unit area (column 3) are calculated for each configuration by summing the individual interfacial energy contributions. Equivalent requirements for stability of each configuration are provided in column 4.

Interface	Configuration	Total interface energy per unit area	Equivalent Criteria		
Oil-Solid-Air	*A1* Dry	$E_{A1} = r\,\gamma_{sa}$	$E_{A1} < E_{A2}, E_{A3}$	$S_{os(a)} < -\gamma_{oa}\left(\frac{r-1}{r-\phi}\right)$	$\theta_{os(a)} > \theta^*$
	A2 Impregnated, emerged	$E_{A2} = (r\text{-}\phi)\gamma_{os} + \phi\,\gamma_{sa} + (1\text{-}\phi)\gamma_{oa}$	$E_{A2} < E_{A1}, E_{A3}$	$-\gamma_{oa}\left(\frac{r-1}{r-\phi}\right) < S_{os(a)} < 0$	$0 < \theta_{os(a)} < \theta^*$
	A3 Encapsulated	$E_{A3} = \gamma_{oa} + r\,\gamma_{os}$	$E_{A1} < E_{A2}, E_{A3}$	$S_{os(a)} \geq 0$	$\theta_{os(a)} = 0$
Oil-Solid-Water	*W1* Impaled	$E_{W1} = r\,\gamma_{sw}$	$E_{W1} < E_{W2}, E_{W3}$	$S_{os(w)} < -\gamma_{ow}\left(\frac{r-1}{r-\phi}\right)$	$\theta_{os(w)} > \theta^*$
	W2 Impregnated, emerged	$E_{W2} = (r\text{-}\phi)\gamma_{os} + \phi\,\gamma_{sw} + (1\text{-}\phi)\gamma_{ow}$	$E_{W2} < E_{W1}, E_{W3}$	$-\gamma_{ow}\left(\frac{r-1}{r-\phi}\right) < S_{os(w)} < 0$	$0 < \theta_{os(w)} < \theta^*$
	W3 Encapsulated	$E_{W3} = \gamma_{ow} + r\,\gamma_{os}$	$E_{W3} < E_{W1}, E_{W2}$	$S_{os(w)} \geq 0$	$\theta_{os(w)} = 0$

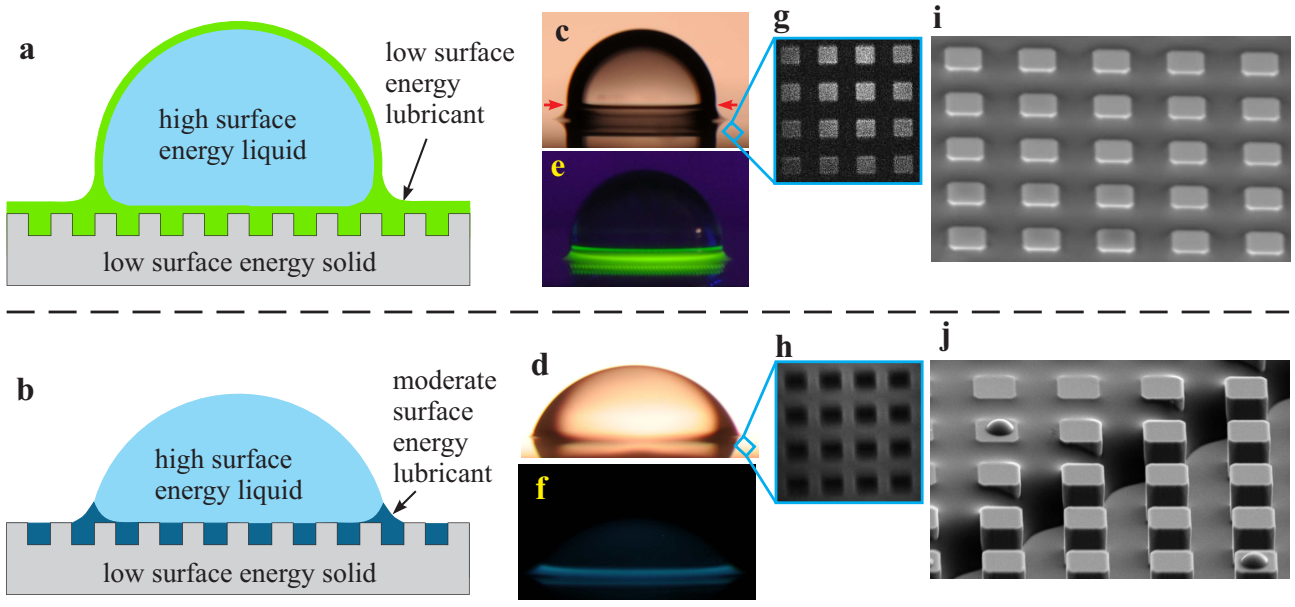

FIG. 1. (a-b) Schematic diagram of a liquid droplet placed on a textured surface impregnated with a lubricant that (a) wets the solid completely, and (b) wets the solid with a non-zero contact angle in the presence of air and the droplet liquid. (c-d) Photographs of a water droplet on a silicon micro post surface (post side a = 10 μm, height h = 10 μm, and spacing b = 10 μm) coated with OTS (octadecyltrichlorosilane) and impregnated with (c) silicone oil, and (d) BMIm respectively. (e-f) Photograph of a water droplet under UV illumination when a fluorescent dye was dissolved in silicone oil and BMIm. The green and blue regions shows that the lubricating oils are pulled up above the texture surface (b = 50 μm). (g-h) Laser confocal fluorescence microscopy (LCFM) images of the impregnated texture show that post tops were bright in the case of silicone oil (g), suggesting that they were covered with oil, and were dark in the case of BMIm (h), suggesting that they were dry. (i) ESEM image of the impregnated texture shows the silicone oil trapped in the texture and suggests that the film that wets the post tops is thin (j) SEM image of the texture impregnated with BMIm shows discrete droplets on post tops indicating that a thin film was not stable in this case.

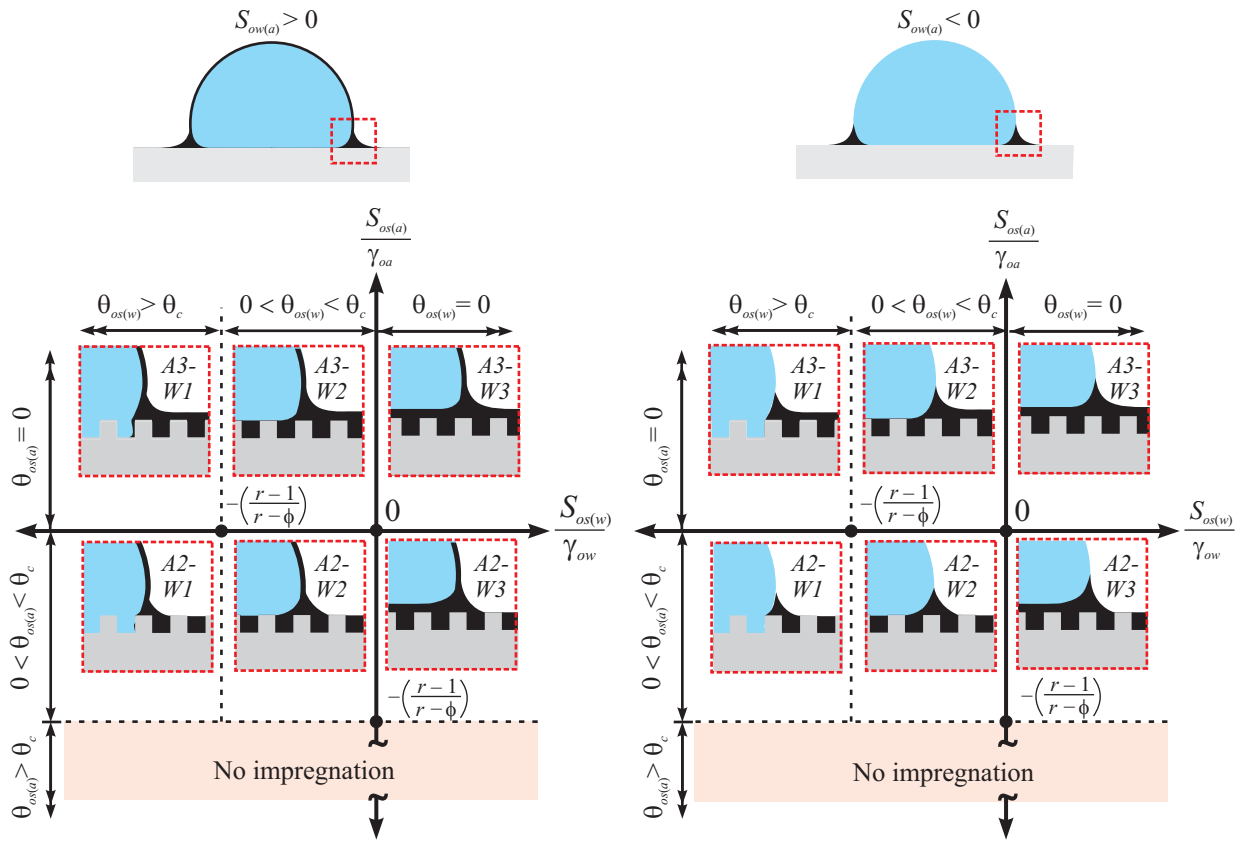

FIG. 2. Possible thermodynamic states of a water droplet placed on a lubricant-encapsulated surface. The top two schematics show whether or not the droplet gets cloaked by the lubricant. For each case, there are six possible states depending on how the lubricant wets the texture in the presence of air (the vertical axis) and water (horizontal axis).

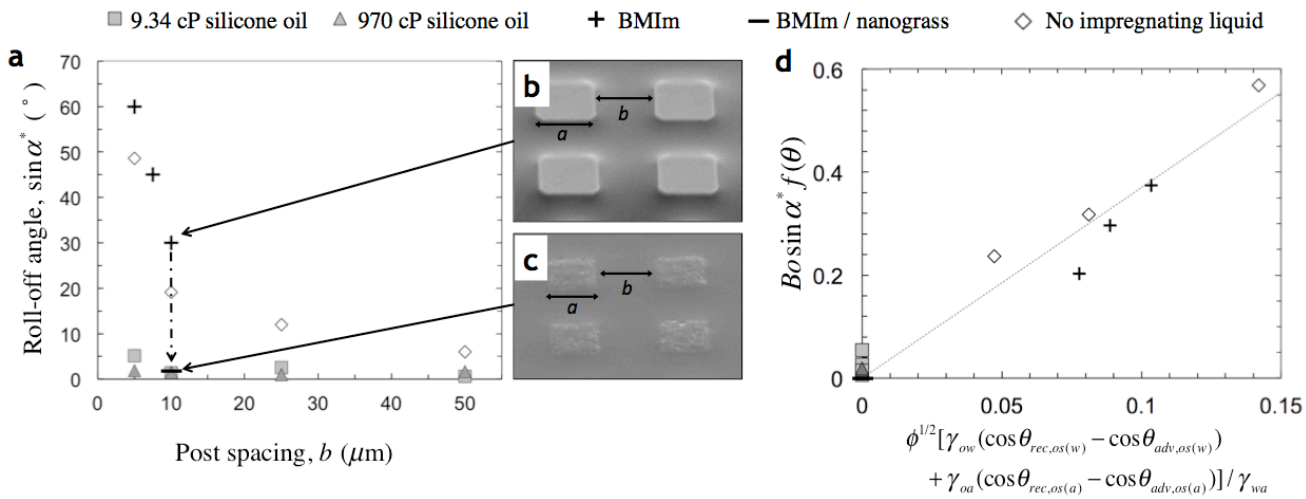

FIG. 3. (a) Measured roll-off angles for different encapsulating liquids as a function of post spacing b. Extremely low roll-off angles are seen in the case of silicone oil impregnated surfaces, consistent with the post tops being encapsulated both outside and underneath the droplet (state *A3-W3*, $\theta_{os(a)}$, $\theta_{os(w)}$ = 0). The high roll-off angles seen in the case of BMIm impregnated surfaces are consistent with the post tops being emergent outside and underneath the droplet (state *A2-W2*, $\theta_c > \theta_{os(a)}, \theta_{os(w)} > 0$). (b) The top inset shows an SEM image of the BMIm impregnated texture and reveals that the post tops are dry. (c) When the posts are further roughened by adding nanograss, they are covered with BMIm (bottom inset) and consequently, the roll-off angle decreases. (b) Non-dimensional plot of scaled gravitational force (left side of Eq. (11)) at the instant of roll-off as a function of the relevant pinning force (right side of Eq. (11)) shows that the roll-off data is in general agreement with the scaling.

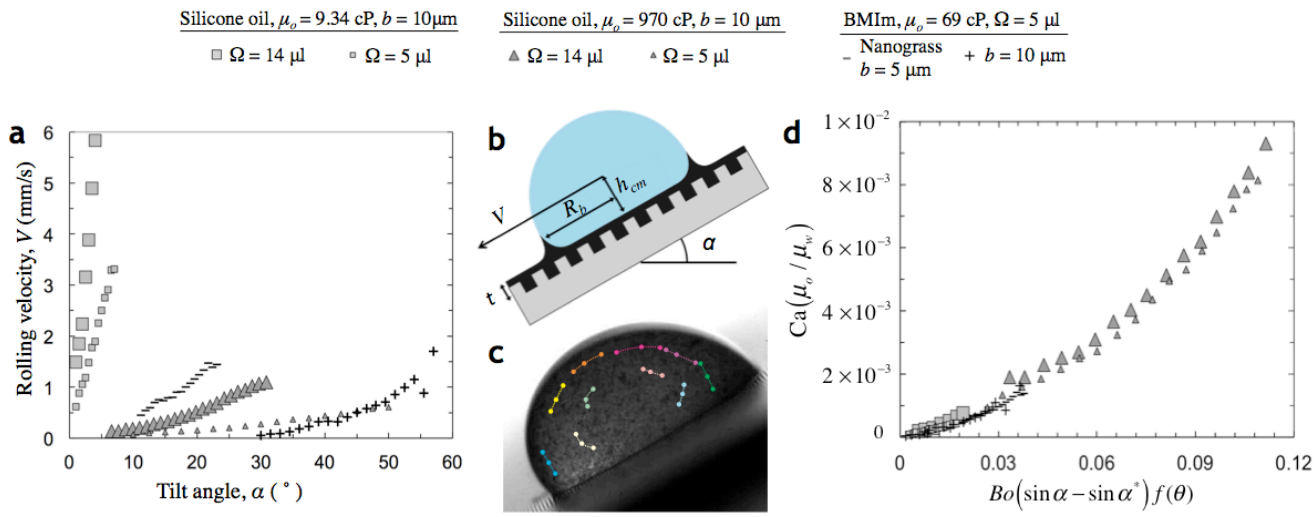

FIG. 4. (a) Measured velocities of water droplets as a function of substrate tilt angle for various lubricant viscosities, post spacings, and droplet sizes (also see supplementary video S1). (b) Schematic of a water droplet moving on a lubricant-impregnated surface showing the various parameters considered in our scaling model. (c) Trajectories of a number of coffee particles measured relative to the water droplet reveal that the drop rolls rather than slips across the surface (also see supplementary video S2). (d) Non-dimensional plot from our model collapses the datasets shown in (a) onto a single curve indicating that the model captures the main physics of the problem.